Fast-Forward Solvers for the Low-Frequency Detection of Buried Dielectric Objects

Tie Jun Cui, *Senior Member, IEEE*, Weng Cho Chew, *Fellow, IEEE*, Alaeddin A. Aydiner, *Student Member, IEEE*, and Yunhua H. Zhang, *Member, IEEE*

***Abstract*—It is known that the extended Born approximation (ExBorn) is much faster than the method of moments (MoM) in the study of electromagnetic scattering by three-dimensional (3-D) dielectric objects, while it is much more accurate than the Born approximation at low frequencies. Hence, it is more applicable in the low-frequency numerical simulation tools. However, the conventional ExBorn is still too slow to solve large-scale problems because it requires $O(N^2)$ computational load, where N is the number of unknowns. In this paper, a fast ExBorn algorithm is proposed for the numerical simulation of 3-D dielectric objects buried in a lossy earth. When the buried objects are discretized with uniform rectangular mesh and the Green's functions are extended appropriately, the computational load can be reduced to $O(N \log N)$ using the cyclic convolution, cyclic correlation, and fast Fourier transform (FFT). Numerical analysis shows that the fast ExBorn provides good approximations if the buried target has a small or moderate contrast. If the contrast is large, however, ExBorn will be less accurate. In this case, a preconditioned conjugate-gradient FFT (CG-FFT) algorithm is developed, where the solution of the fast ExBorn is chosen as the initial guess and the preconditioner. Numerical results are given to test the validity and efficiency of the fast algorithms.**

***Index Terms*—Buried objects, conjugate-gradient fast Fourier transform (CG-FFT) algorithm, cyclic convolution, cyclic correlation, fast extended Born approximation, half space, low-frequency numerical simulation.**

I. Introduction

IT IS VERY important to seek fast solutions to electromagnetic scattering and inverse scattering by dielectric objects buried in a lossy earth. Such topic has found wide applications in the near-surface geophysical exploration, environmental science, as well as demining, detection, and characterization of unexploded ordnance. Usually, a ground-penetrating radar (GPR) is the electromagnetic tool of choice for the detection problem because it can provide high-resolution images [2]–[5]. Unfortunately, when the electrical conductivity of the lossy ground is high, as in typical wet soils and clay caps, the GPR cannot penetrate deep enough for many applications due to its high-frequency components [5]. In order to achieve greater penetration in the conductive earth, much lower frequencies are used in the time-domain electromagnetic induction tool [6], which operates at low enough frequencies such that the diffusion rather than the wave propagation governs the induced earth currents and the resulting fields. However, a loss of resolution often accompanies the induction tool. To fill the gap between the GPR and the induction tool, a very early time electromagnetic (VETEM) system has been proposed [7], [8], which works in the frequency range from zero to several megahertz. Hence, efficient full-wave simulation methods are required in such frequency range to analyze the VETEM system.

In the analysis of electromagnetic scattering by three-dimensional (3-D) inhomogeneous dielectric objects buried in the lossy earth, several approaches have been developed to solve the volume electric-field integral equation, for example, the conventional method of moments (MoM) [9], [10], the conjugate-gradient fast Fourier transform (CG-FFT) algorithms [11]–[14], and the extended Born approximation (ExBorn) [15]–[18], [20]. In these methods, MoM requires $O(N^2)$ memory usage and $O(N^3)$ computational load to solve the matrix equation using the LU decomposition or Gaussian elimination, where N is the number of unknowns. Hence, MoM can only be used to solve small problems.

The CG-FFT algorithm is one of the most efficient ways to solve the volume integral equation for buried dielectric objects [14]. When the buried objects are discretized with uniform rectangular mesh, the required floating-point operations are only proportional to $C_1 N_{\text{iter}} N \log N$. Here, C_1 is a constant and N_{iter} is the number of iterations. However, the convergence of CG-FFT is very slow at low frequencies [19], and the constant C_1 is relatively high. Thus, the CG-FFT algorithm is still not fast enough for very-large scale problems.

The extended Born approximation, which was originally proposed by Habashy *et al.* [1], is an efficient method to solve moderately sized problems. Later, the method is well developed by Torres-Verdin and Habashy [15]–[17], Yu and Carin [18], and Liu and Zhang [20]. It has proven that ExBorn is very accurate at low frequencies, and the computational complexity has been reduced from $O(N^3)$ to $O(N^2)$. However, the conventional ExBorn is still slow for very large problems. Recently, a fast ExBorn algorithm has been proposed to solve two-dimensional (2-D) scalar integral equations with homogeneous

Manuscript received February 27, 2002; revised March 8, 2003. This work was supported by the Department of Energy under Grant DOE DEFG07-97ER 14835, by the Air Force Office of Scientific Research under MURI Grant F49620-96-1-0025, and by the National Science Foundation under Grant NSF ECS 99-06651. The work of T. J. Cui was supported by the National Science Foundation of China for Distinguished Young Scholars under Grant 60225001, China.

T. J. Cui is with the Center for Computational Electromagnetics and the State Key Laboratory of Millimeter Waves, Department of Radio Engineering, Southeast University, Nanjing 210096, China.

W. C. Chew and A. A. Aydiner are with the Center for Computational Electromagnetics and the Electromagnetic Laboratory, Department of Electrical and Computer Engineering, University of Illinois at Urbana-Champaign, Urbana, IL 61801-2991 USA.

Y. H. Zhang is with the Center for Space Science and Applied Research, Chinese Academy of Science, Beijing, China.

Digital Object Identifier 10.1109/TGRS.2003.813502

Green's kernel using FFT [20]. Here, the computational complexity is only of $O(N \log N)$ if the object is discretized with uniform rectangular mesh. In order to use this idea to solve 3-D numerical simulation problems, however, the following difficulties must be handled: 1) replacing the free-space scalar Green's function by half-space dyadic Green's functions; 2) solving 3-D vector integral equations instead of solving the 2-D scalar integral equation at the cost of $O(N \log N)$.

In this paper, we will solve the above difficulties. For 3-D numerical simulation problems, general formulations are derived when the transmitter and receiver are electric and magnetic dipoles. Here, five Sommerfeld integrals are involved and the symmetrical property has been found in the half-space dyadic Green's functions. Such symmetrical property will save one-third of the memory requirement and the CPU time. Based on the general formulations, a fast ExBorn algorithm is developed for 3-D numerical simulation problems when the buried object is discretized with uniform rectangular mesh. After extending the half-space dyadic Green's functions appropriately, the required floating-point operations are proportional to $C_2 N \log N$ using the cyclic convolution, cyclic correlation, and FFT. Comparing with the CG-FFT algorithm, the fast ExBorn algorithm is much more efficient because $C_1 N_{\text{iter}}$ is much larger than C_2. Numerical analysis shows that the fast ExBorn is very accurate when the contrast of target is small or relatively large, and becomes less accurate when the contrast is large. In the later case, a preconditioned CG-FFT algorithm is presented, which is much faster than the conventional one. In the preconditioned CG-FFT algorithm, the solution of the fast ExBorn is chosen as the initial guess and the preconditioner. Numerical results are given to test the validity and efficiency of the fast algorithms.

II. General Formulations

Let us consider a general case in the buried object problem. The transmitter (TX) and receiver (RX) are arbitrarily oriented electric dipole or magnetic dipole. The orientation direction of TX is $\hat{\alpha}_t$, and the orientation direction of RX is $\hat{\alpha}_r$. Both TX and RX are located in the upper space, Region a, which is characterized by the relative permittivity ϵ_a and the conductivity σ_a. Usually, $\epsilon_a = 1$ and $\sigma_a = 0$ for the case of the air. The buried dielectric object, which is characterized by the relative permittivity ϵ_s and the conductivity σ_s, is located in the lossy earth, Region b, which is characterized by the relative permittivity ϵ_b and the conductivity σ_b. A Cartesian coordinate system is adopted, where the origin is located at the air–earth interface and the z axis is perpendicular to the interface toward the air.

The electric field excited by the transmitter in Region b is just the incident field of the buried object. Using the half-space dyadic Green's functions [22], we easily obtain the incident electric field. For the case of the electric-dipole transmitter, we have

$$\mathbf{E}_b^{\text{inc}}(\mathbf{r}, \mathbf{r}_t) = -\frac{\eta_0}{k}(I\Delta l)\overline{\mathbf{G}}_{ee}^{ba}(\mathbf{r}, \mathbf{r}_t) \cdot \hat{\alpha}_t. \tag{1}$$

For the case of the magnetic-dipole (small-loop) transmitter, we have

$$\mathbf{E}_b^{\text{inc}}(\mathbf{r}, \mathbf{r}_t) = -i\frac{\eta_0}{k}(IA)\overline{\mathbf{G}}_{em}^{ba}(\mathbf{r}, \mathbf{r}_t) \cdot \hat{\alpha}_t. \tag{2}$$

Here, k and η_0 are the wavenumber and wave impedance in the free space; $I\Delta l$ and IA represent the moments of electric and magnetic dipoles; and $\overline{\mathbf{G}}_{ee}^{ba}$ and $\overline{\mathbf{G}}_{em}^{ba}$ are spatial-domain electric-field dyadic Green's functions when the observation point is in Region b and the source point is in Region a. In [22], closed-form expressions for the spectral-domain dyadic Green's functions have been given for the electric dipole and magnetic dipole. After simple derivations, the spatial-domain dyadic Green's functions can be expressed by Sommerfeld integrals

$$\overline{\mathbf{G}}_{ee}^{ba}(\mathbf{r}, \mathbf{r}') = \frac{1}{2\pi}\begin{bmatrix} g_7^e + \overline{Y}^2 g_6^e & -\overline{XY} g_6^e & i\overline{x} g_3^e \\ -\overline{XY} g_6^e & g_7^e + \overline{X}^2 g_6^e & i\overline{y} g_3^e \\ i\overline{x} g_4^e & i\overline{y} g_4^e & g_5^e \end{bmatrix} \tag{3}$$

$$\overline{\mathbf{G}}_{em}^{ba}(\mathbf{r}, \mathbf{r}') = \frac{1}{2\pi}\begin{bmatrix} \overline{XY} g_1^m & g_6^m + \overline{Y}^2 g_1^m & -i\overline{y} g_5^m \\ -g_6^m - \overline{X}^2 g_1^m & -\overline{XY} g_1^m & i\overline{x} g_5^m \\ i\tilde{\epsilon}_a \overline{y} g_4^m & -i\tilde{\epsilon}_a \overline{x} g_4^m & 0 \end{bmatrix} \tag{4}$$

where $\overline{X} = \overline{x}/\rho$, $\overline{Y} = \overline{y}/\rho$, $\overline{x} = x - x'$, $\overline{y} = y - y'$, and $\rho^2 = \overline{x}^2 + \overline{y}^2$. In above equations, $g_i^e (i = 1, 2, \ldots, 7)$ and $g_j^m (j = 1, 2, \ldots, 6)$ are Sommerfeld integrals, which satisfy $g_6^e = g_5^e - 2g_2^e$, $g_7^e = g_1^e + g_2^e$, and $g_6^m = g_3^m - g_2^m$. Hence, only five independent Sommerfeld integrals are involved in both cases

$$g_n^{e,m} = \int_0^{+\infty} dk_s k_s \tilde{g}_n^{e,m} e^{i(k_{az} z' - k_{bz} z)}, \quad (n = 1, 2, \ldots, 5) \tag{5}$$

in which

$$\begin{aligned} \tilde{g}_1^e &= k_{az} k_{bz} g_0 f_0, \quad \tilde{g}_2^e = k_s g_0 f_1, \quad \tilde{g}_3^e = k_s k_{bz} g_0 f_1 \\ \tilde{g}_4^e &= k_s k_{az} g_0 f_1, \quad \tilde{g}_5^e = k_s^2 g_0 f_0 \end{aligned} \tag{6}$$

$$\begin{aligned} \tilde{g}_1^m &= k_s g_1 f_2, \quad \tilde{g}_2^m = k^2 g_2 f_0, \quad \tilde{g}_3^m = k_s g_1 f_1 \\ \tilde{g}_4^m &= k_s k^2 g_0 f_1, \quad \tilde{g}_5^m = k_s k^2 g_3 f_1. \end{aligned} \tag{7}$$

Here

$$\begin{aligned} f_0 &= J_0(k_s\rho) \quad f_1 = J_1(k_s\rho)/\rho \\ f_2 &= [k_s\rho J_0(k_s\rho) - 2J_1(k_s\rho)]/\rho \end{aligned}$$

are Bessel-related functions, and $g_0 = 1/(\tilde{\epsilon}_a k_{bz} + \tilde{\epsilon}_b k_{az})$, $g_1 = (k_{bz} - k_{az}) g_0$, $g_2 = \tilde{\epsilon}_a k_{bz} g_0$, $g_3 = 1/(k_{bz} + k_{az})$. In these equations, $\tilde{\epsilon}_{a,b} = \epsilon_{a,b} + i\eta_0 \sigma_{a,b}/k$ denotes the complex permittivity, and $k_{az,bz}^2 = k^2 \tilde{\epsilon}_{a,b} - k_s^2$.

We remark that the integrand of the Sommerfeld integral (5) decays very fast when the observation point and/or the source point are far away from the air–earth interface, i.e., $z' \gg 0$ and/or $-z \gg 0$. If both the observation and source points are close to the air–earth interface, however, (5) tends to be a slowly convergent integral. When the observation and source points are both located at the interface ($z = z' = 0$), the exponential decay along the z direction disappears and the Sommerfeld integral

becomes divergent. Usually, the third case is not considered because we can always suppose that the buried object is a little bit below the air–earth interface.

In the numerical evaluation of the Sommerfeld integral, we first set a small threshold parameter δ. Let

$$\left|e^{i(k_{az}z'-k_{bz}z)}\right| \le \delta.$$

Then, the interval of integrating $k_s^{\max}$ is determined. By choosing different threshold, we can control the accuracy of the numerical integration. In this paper, we choose $\delta = 10^{-8}$. The computation of Sommerfeld integrals may be time consuming because large amount of Sommerfeld integrals need to be computed for different transmitter locations and many observation points inside the buried object. Hence, the Sommerfeld integrals are usually precomputed and stored as a table for a list of ρ and z before solving the integral equation. Then the interpolation is used to obtain the Sommerfeld integrals rapidly for different transmitter locations and different observation points in the fast algorithms.

Under the illumination of the incident electric field, the total electric field inside the dielectric object, $\mathbf{E}_b$, can be determined through the following volume integral equation

$$\mathbf{E}_b(\mathbf{r},\mathbf{r}_t) + \frac{1}{4\pi\tilde{\epsilon}_b}\int_V d\mathbf{r}'\overline{\mathbf{G}}_{ee}^{bb}(\mathbf{r},\mathbf{r}') \cdot[\tilde{\epsilon}_s(\mathbf{r}')-\tilde{\epsilon}_b]\,\mathbf{E}_b(\mathbf{r}',\mathbf{r}_t) = \mathbf{E}_b^{\rm inc}(\mathbf{r},\mathbf{r}_t) \quad (8)$$

where V is a box region containing the buried dielectric object, and $\overline{\mathbf{G}}_{ee}^{bb}$ is the half-space electric-field dyadic Green's function when the source and observation points are both in Region b. In [14] and [22], a symmetrical form of the Green's function has been proposed where the nabla operators can be transferred to the testing and basis functions when applying MoM. Here, we will provide its matrix version to use the extended Born approximation. From the symmetrical form of the Green's function [14], [22], one easily obtains

$$\overline{\mathbf{G}}_{ee}^{bb}(\mathbf{r},\mathbf{r}') = \overline{\mathbf{G}}_{ee}^{bbP}(\mathbf{r},\mathbf{r}') - \overline{\mathbf{G}}_{ee}^{bbI}(\mathbf{r},\mathbf{r}') + \overline{\mathbf{G}}_{ee}^{bbT}(\mathbf{r},\mathbf{r}') \quad (9)$$

where

$$\overline{\mathbf{G}}_{ee}^{bbP}(\mathbf{r},\mathbf{r}') = \frac{e^{ik_bR}}{R^5}\begin{bmatrix} q+\overline{x}^2p & \overline{x}\overline{y}p & \overline{x}\overline{z}p \\ \overline{x}\overline{y}p & q+\overline{y}^2p & \overline{y}\overline{z}p \\ \overline{x}\overline{z}p & \overline{y}\overline{z}p & q+\overline{z}^2p \end{bmatrix} \quad (10)$$

is the contribution from the primary field (i.e., the dyadic Green's function in homogenous space when the interface does not exist), in which $\overline{z} = z - z'$, $R^2 = \rho^2 + \overline{z}^2$, $p = k_b^2R^2 + i3k_bR - 3$, and $q = -R^2(k_b^2R^2 + ik_bR - 1)$; $\overline{\mathbf{G}}_{ee}^{bbI}$ is the contribution from the image field which can be determined through (10) by replacing $z - z'$ with $z + z'$; and $\overline{\mathbf{G}}_{ee}^{bbT}$ is expressed by Sommerfeld integrals

$$\overline{\mathbf{G}}_{ee}^{bbT}(\mathbf{r},\mathbf{r}') = \frac{1}{2\pi}\begin{bmatrix} I_7^e+\overline{Y}^2I_6^e & -\overline{XY}I_6^e & it\overline{x}I_3^e \\ -\overline{XY}I_6^e & I_7^e+\overline{X}^2I_6^e & it\overline{y}I_3^e \\ i\overline{x}I_4^e & i\overline{y}I_4^e & tI_5^e \end{bmatrix} \quad (11)$$

in which $t = \tilde{\epsilon}_a/\tilde{\epsilon}_b$, $I_6^e = I_5^e - 2I_2^e$, and $I_7^e = I_1^e + I_2^e$. Hence, five independent Sommerfeld integrals are involved in the above spatial-domain Green's function

$$I_n^e = \int_0^{+\infty} dk_s k_s \tilde{g}_n^e e^{-ik_{bz}(z+z')}, \quad (n = 1, 2, \ldots, 5). \quad (12)$$

Here, $\tilde{g}_n^e$ is exactly the same as defined in (6). The computation of the Sommerfeld integral (12) is similar to that of (5), as discussed before.

In fact, the summation of the last two terms in the dyadic Green's function (9) are just the contribution from the reflected field [9], [10], i.e., $\overline{\mathbf{G}}_{ee}^{bbR} = -\overline{\mathbf{G}}_{ee}^{bbI} + \overline{\mathbf{G}}_{ee}^{bbT}$. The reason why we write it in the form of (9) is because the evaluation of Sommerfeld integrals involved in (11) is much easier and more accurate than that in [9], [10]. Thus, the dyadic Green's function $\overline{\mathbf{G}}_{ee}^{bb}$ can be rewritten as

$$\overline{\mathbf{G}}_{ee}^{bb}(\mathbf{r},\mathbf{r}') = \overline{\mathbf{G}}_{ee}^{bbP}(\mathbf{r},\mathbf{r}') + \overline{\mathbf{G}}_{ee}^{bbR}(\mathbf{r},\mathbf{r}'). \quad (13)$$

If we use $G_{\xi\zeta}^{P,R}(\xi,\zeta = x,y,z)$ to represent the matrix elements of $\overline{\mathbf{G}}_{ee}^{bbP,R}$, we will obtain the following symmetric or antisymmetric property from (10) and (11):

$$\begin{aligned} &G_{yx}^P = G_{xy}^P \quad G_{zx}^P = G_{xz}^P \quad G_{zy}^P = G_{yz}^P \\ &G_{yx}^R = G_{xy}^R \quad G_{zx}^R = -G_{xz}^R \quad G_{zy}^R = -G_{yz}^R \end{aligned}$$

which can also be easily derived from a physical sketch in terms of reflecting plane waves. Hence, there are only six independent elements in both matrices $\overline{\mathbf{G}}_{ee}^{bbP}$ and $\overline{\mathbf{G}}_{ee}^{bbR}$. Such feature will save one-third of the memory requirement and CPU time in the fast-ExBorn implementation introduced in the next section. Also, there are only four independent Sommerfeld integrals I_1^e, I_2^e, I_3^e, and I_5^e involved in the dyadic Green's function.

Equation (8) is the integral equation for the internal electric field $\mathbf{E}_b$. In fact, it has two equivalent versions for the induced current $\mathbf{J}_b$ and the electric displacement $\mathbf{D}_b$

$$\mathbf{J}_b(\mathbf{r},\mathbf{r}_t) + \frac{1}{4\pi}\chi(\mathbf{r})\int_V d\mathbf{r}'\overline{\mathbf{G}}_{ee}^{bb}(\mathbf{r},\mathbf{r}') \cdot\mathbf{J}_b(\mathbf{r}',\mathbf{r}_t) = \mathbf{J}_b^{\rm inc}(\mathbf{r},\mathbf{r}_t) \quad (14)$$

$$\mathbf{D}_b(\mathbf{r},\mathbf{r}_t) + \frac{1}{4\pi\tilde{\epsilon}_b}\tilde{\epsilon}_s(\mathbf{r})\int_V d\mathbf{r}'\overline{\mathbf{G}}_{ee}^{bb}(\mathbf{r},\mathbf{r}') \cdot[1-\tilde{\epsilon}_b/\tilde{\epsilon}_s(\mathbf{r}')]\mathbf{D}_b(\mathbf{r}',\mathbf{r}_t) = \mathbf{D}_b^{\rm inc}(\mathbf{r},\mathbf{r}_t) \quad (15)$$

where $\chi(\mathbf{r}) = \tilde{\epsilon}_s(\mathbf{r})/\tilde{\epsilon}_b - 1$, and

$$\begin{aligned} \mathbf{J}_b(\mathbf{r},\mathbf{r}_t) &= \chi(\mathbf{r})\mathbf{E}_b(\mathbf{r},\mathbf{r}_t) \\ \mathbf{J}_b^{\rm inc}(\mathbf{r},\mathbf{r}_t) &= \chi(\mathbf{r})\mathbf{E}_b^{\rm inc}(\mathbf{r},\mathbf{r}_t) \end{aligned} \quad (16)$$

are the normalized electric current inside the buried object and the equivalent incident current, respectively, and

$$\begin{aligned} \mathbf{D}_b(\mathbf{r},\mathbf{r}_t) &= \tilde{\epsilon}_s(\mathbf{r})\mathbf{E}_b(\mathbf{r},\mathbf{r}_t) \\ \mathbf{D}_b^{\rm inc}(\mathbf{r},\mathbf{r}_t) &= \tilde{\epsilon}_s(\mathbf{r})\mathbf{E}_b^{\rm inc}(\mathbf{r},\mathbf{r}_t) \end{aligned} \quad (17)$$

are the electric displacement inside the buried object and the equivalent electric displacement, respectively.

After the total electric field is obtained by solving the integral equation (8) or (14) or (15), as shown in the next section, the scattered electric field received by the electric dipole or the magnetic field received by the magnetic dipole is written as

$$\hat{\alpha}_r \cdot \mathbf{E}_a^{\rm sca}(\mathbf{r}_r, \mathbf{r}_t, k) = i \int_V d\mathbf{r} \hat{\alpha}_r \cdot \overline{\mathbf{G}}_{ee}^{ab}(\mathbf{r}_r, \mathbf{r}) \cdot \mathbf{E}_b(\mathbf{r}, \mathbf{r}_t)\left[\tilde{\epsilon}_s(\mathbf{r}) - \tilde{\epsilon}_b\right] \tag{18}$$

$$\hat{\alpha}_r \cdot \mathbf{H}_a^{\rm sca}(\mathbf{r}_r, \mathbf{r}_t, k) = \frac{i}{k\eta_0} \int_V d\mathbf{r} \hat{\alpha}_r \cdot \overline{\mathbf{G}}_{me}^{ab}(\mathbf{r}_r, \mathbf{r}) \cdot \mathbf{E}_b(\mathbf{r}, \mathbf{r}_t)\left[\tilde{\epsilon}_s(\mathbf{r}) - \tilde{\epsilon}_b\right] \tag{19}$$

where the electric-field and magnetic-field dyadic Green's functions $\overline{\mathbf{G}}_{ee}^{ab}$ and $\overline{\mathbf{G}}_{me}^{ab}$ are easily determined from the reciprocity theorem

$$\overline{\mathbf{G}}_{ee}^{ab}(\mathbf{r}, \mathbf{r}') = \left[\overline{\mathbf{G}}_{ee}^{ba}(\mathbf{r}', \mathbf{r})\right]^t \tag{20}$$

$$\overline{\mathbf{G}}_{me}^{ab}(\mathbf{r}, \mathbf{r}') = -\left[\overline{\mathbf{G}}_{em}^{ba}(\mathbf{r}', \mathbf{r})\right]^t \tag{21}$$

in which "t" denotes a matrix transpose. The above relations can also be verified using the Sommerfeld integrals.

III. Fast ExBorn Algorithm

If the volume integral equations (8), (14) and (15) are solved using the conventional MoM with the LU decomposition or Gaussian elimination, the arithmetic operations will be as the order of $O(N^3)$. Hence, the direct MoM method is very slow. Considering the fact that the Green's function in the integral equation is very large for $\mathbf{r}'$ located at the vicinity of $\mathbf{r}$, and is very small for $\mathbf{r}'$ distant from $\mathbf{r}$ due to the kernel $\exp(ik_b|\mathbf{r}-\mathbf{r}'|)/|\mathbf{r}-\mathbf{r}'|$, the Green's function behaves approximately like a Dirac-δ function. Using the property of Dirac-δ function, (8), (14) and (15) can be approximately written as

$$\left[\overline{\mathbf{I}} + \overline{\mathbf{A}}(\mathbf{r}, \mathbf{r}_t)\right] \cdot \mathbf{E}_b(\mathbf{r}, \mathbf{r}_t) = \mathbf{E}_b^{\rm inc}(\mathbf{r}, \mathbf{r}_t) \tag{22}$$

where $\overline{\mathbf{I}}$ is a unit matrix and

$$\overline{\mathbf{A}}(\mathbf{r}, \mathbf{r}_t) = \frac{1}{4\pi\tilde{\epsilon}_b} C(\mathbf{r}) \int_V d\mathbf{r}' \overline{\mathbf{G}}_{ee}^{bb}(\mathbf{r}, \mathbf{r}') O(\mathbf{r}') \tag{23}$$

is a 3×3 matrix. Equation (22) is a general form of the extended Born approximation [1], [15]–[18], [20], [21]. Here, $C(\mathbf{r}) = 1$ and $O(\mathbf{r}) = \tilde{\epsilon}_s(\mathbf{r}) - \tilde{\epsilon}_b$ for (8), $C(\mathbf{r}) = \tilde{\epsilon}_s(\mathbf{r}) - \tilde{\epsilon}_b$ and $O(\mathbf{r}) = 1$ for (14), and $C(\mathbf{r}) = \tilde{\epsilon}_s(\mathbf{r})$ and $O(\mathbf{r}) = 1 - \tilde{\epsilon}_b/\tilde{\epsilon}_s(\mathbf{r})$ for (15). In all cases, $C(\mathbf{r})O(\mathbf{r}) = \tilde{\epsilon}_s(\mathbf{r}) - \tilde{\epsilon}_b$ is a constant function. From (22), the extended Born approximation will be reduced to the Born approximation when $\overline{\mathbf{A}}(\mathbf{r}, \mathbf{r}_t) = \overline{\mathbf{0}}$.

We remark that the extended Born approximation is particularly good for the low-frequency and lossy case. At low frequencies, the imaginary part of the complex permittivity in the lossy earth ($\tilde{\epsilon}_b = \epsilon_b + i\eta_0\sigma_b/k$) is very high. Hence, the kernel $\exp(ik_b|\mathbf{r}-\mathbf{r}'|)/|\mathbf{r}-\mathbf{r}'|$ will keep the very high value (in fact singular) when $\mathbf{r}' \to \mathbf{r}$, and will decrease exponentially when $\mathbf{r}'$ is distant from $\mathbf{r}$ due to the large attenuation. Therefore, the Green's function behaves more like a Dirac-δ function than that in lossless case.

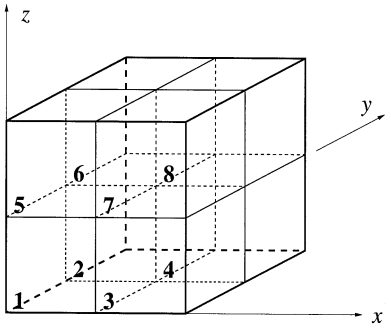

Fig. 1. Extended domain of the Green's functions, in which Domain 1 is the original computational domain.

From (22), we clearly see that the total electric field $\mathbf{E}_b$ can be easily obtained by solving a 3×3 matrix equation. However, the evaluation of matrix $\overline{\mathbf{A}}$ requires $9N^2$ computational load for all observation points. Thus, the conventional ExBorn algorithm is still expensive. To accelerate the evaluation of matrix $\overline{\mathbf{A}}$, we rewrite (23) in a component form as

$$A_{\xi\zeta}(\mathbf{r}) = \frac{1}{4\pi\tilde{\epsilon}_b} C(\mathbf{r}) \int_V d\mathbf{r}' G_{\xi\zeta}(\mathbf{r}, \mathbf{r}') O(\mathbf{r}') \tag{24}$$

in which $\xi = x, y, z$, $\zeta = x, y, z$, and the Green's function $G_{\xi\zeta}(\mathbf{r}, \mathbf{r}')$ contains two parts contributed from the primary field and the reflected field

$$G_{\xi\zeta}(\mathbf{r}, \mathbf{r}') = G_{\xi\zeta}^P(x - x', y - y', z - z') + G_{\xi\zeta}^R(x - x', y - y', z + z'). \tag{25}$$

From (24) and (25), one easily recognizes convolutions and correlations amongst continuous functions. In order to compute the convolution and correlation via FFT, we discretize the box region of the buried object V by regular cuboidal lattices labeled as (i_x, i_y, i_z) with $i_{x,y,z} = 0, 1, \ldots, N_{x,y,z} - 1$. Then, the matrix element (24) can be written in a discretized form as

$$\begin{aligned} A_{\xi\zeta}(i_x, i_y, i_z) &= \frac{\Delta V}{4\pi\tilde{\epsilon}_b} C(i_x, i_y, i_z) \sum_{i_x'=0}^{N_x-1} \sum_{i_y'=0}^{N_y-1} \sum_{i_z'=0}^{N_z-1} \\ &\cdot \left[G_{\xi\zeta}^P(i_x - i_x', i_y - i_y', i_z - i_z') O(i_x', i_y', i_z') \right. \\ &\left. + G_{\xi\zeta}^R(i_x - i_x', i_y - i_y', i_z + i_z') O(i_x', i_y', i_z')\right]. \end{aligned} \tag{26}$$

Clearly, the first term on the right-hand side of (26) looks like a 3-D cyclic convolution in $\hat{x}$, $\hat{y}$, and $\hat{z}$ directions, and the second term looks like a 2-D cyclic convolution in $\hat{x}$ and $\hat{y}$ directions and a one-dimensional (1-D) cyclic correlation in the $\hat{z}$ direction. However, the above two terms are indeed not the cyclic convolution and correlation because the Green's functions do not satisfy the cyclic property in the original computational domain $N_x \times N_y \times N_z$.

The computations of the summation similar to (26) via FFT have been discussed many times in the literature for both the free-space case [11], [12], [23] and the half-space case [14], [24]. In these computations, the knowledge of Green's functions in an extended domain which is twice the original one in each direction is required. Fig. 1 illustrates the original domain,

TABLE I
SIGNS OF THE GREEN'S FUNCTIONS ($G^P_{\xi\zeta}$, $\xi, \zeta = x, y, z$) CONTRIBUTED BY THE PRIMARY FIELD IN DIFFERENT EXTENDED SUBDOMAINS

subdomain	# 1	# 2	# 3	# 4	# 5	# 6	# 7	# 8
x-direction	ori. x	ori. x	ext. x	ext. x	ori. x	ori. x	ext. x	ext. x
y-direction	ori. y	ext. y	ori. y	ext. y	ori. y	ext. y	ori. y	ext. y
z-direction	ori. z	ori. z	ori. z	ori. z	ext. z	ext. z	ext. z	ext. z
G^P_{xx}	+	+	+	+	+	+	+	+
G^P_{yy}	+	+	+	+	+	+	+	+
G^P_{zz}	+	+	+	+	+	+	+	+
G^P_{xy}	+	−	−	+	+	−	−	+
G^P_{xz}	+	+	−	−	−	−	+	+
G^P_{yz}	+	−	+	−	−	+	−	+

TABLE II
SIGNS OF THE GREEN'S FUNCTIONS ($G^R_{\xi\zeta}$, $\xi, \zeta = x, y, z$) CONTRIBUTED BY THE REFLECTED FIELD IN DIFFERENT EXTENDED SUBDOMAINS

subdomain	# 1	# 2	# 3	# 4	# 5	# 6	# 7	# 8
x-direction	ori. x	ori. x	ext. x	ext. x	ori. x	ori. x	ext. x	ext. x
y-direction	ori. y	ext. y	ori. y	ext. y	ori. y	ext. y	ori. y	ext. y
z-direction	ori. z	ori. z	ori. z	ori. z	ext. z	ext. z	ext. z	ext. z
G^R_{xx}	+	+	+	+	+	+	+	+
G^R_{yy}	+	+	+	+	+	+	+	+
G^R_{zz}	+	+	+	+	+	+	+	+
G^R_{xy}	+	−	−	+	+	−	−	+
G^R_{xz}	+	+	−	−	+	+	−	−
G^R_{yz}	+	−	+	−	+	−	+	−

Subdomain #1, and the extended domain of the Green's functions in the 3-D case. Actually, the extended Green's functions are nothing else than the wrapped version of the actual Green's functions in the extended domain. The block diagram given in [23, Fig. 13] shows the procedures of such computations.

If the Green's function is a scalar one like that in the 2-D case [23], or is a dyadic one with symmetric forms [11], [12], [14], the extended Green's function can be easily defined [14]. If the dyadic Green's function is expressed by the matrix form, however, different signs must be assigned for different matrix elements in different extended subdomains. For the Green's functions contributed by the primary field, $G^P_{\xi\zeta}$, the extensions are defined as

$$G^{Pe}_{\xi\zeta}(i_x, i_y, i_z) = \pm G^P_{\xi\zeta}(l_x, l_y, l_z) \tag{27}$$

for the Green's functions contributed by the reflected field, $G^R_{\xi\zeta}$, the extensions are defined as

$$G^{Re}_{\xi\zeta}(i_x, i_y, i_z) = \pm G^R_{\xi\zeta}(l_x, l_y, i_z) \tag{28}$$

where $i_\xi = 0, 1, \ldots, 2N_\xi - 1 (\xi = x, y, z)$. When $0 \le i_\xi \le N_\xi - 1$, we have $l_\xi = i_\xi$; when $N_\xi \le i_\xi \le 2N_\xi - 1$, we have $l_\xi = 2N_\xi - i_\xi$. Tables I and II list the signs of the extended Green's functions $G^{Pe}_{\xi\zeta}$ and $G^{Re}_{\xi\zeta}$ in the eight subdomains shown in Fig. 1, respectively.

From Tables I and II, we clearly see that the signs of the Green's functions are directly related to the even and odd nature of the components with respect to the coordinates in different extended subdomains. In subdomain #1, the original computational domain, all components of Green's functions keep their original forms, which is obvious.

For the diagonal terms of the dyadic Green's function contributed by the primary field, G^P_{xx}, G^P_{yy}, and G^P_{zz}, they are even functions of the coordinates $x - x'$, $y - y'$, and $z - z'$, respectively, as shown in (10). These terms are unchanged if we exchange the roles of (x, y, z) and (x', y', z'). Hence, they will keep the original signs in all extended subdomains, as illustrated in Table I. For nondiagonal terms, however, the signs will be different in different extended subdomains. For example, let us consider subdomain #6. From Fig. 1, the x coordinate keeps the original but the y and z coordinates are extended in this subdomain. Hence, the matrix component G^P_{xy}, which is an odd function of $x - x'$ and $y - y'$, will keep the sign in $x - x'$ and change the sign in $y - y'$. Therefore, the sign of G^P_{xy} will be changed. Similarly, the matrix component G^P_{xz} will change the sign but G^P_{yz} will keep the sign in this subdomain. Using the same way, the signs of G^P_{xy}, G^P_{xz}, and G^P_{yz} in all subdomains are easily determined, as shown in Table I.

All of the matrix components of the dyadic Green's function contributed by the reflected field are related to $z + z'$ through the Sommerfeld integral (12). When we exchange the roles of z and z', all components will keep the same. Hence, they can be regarded as a generalized even function of $z + z'$. As a result of this observation, the diagonal terms G^R_{xx}, G^R_{yy}, and G^R_{zz} will keep the original signs in all extended subdomains, as illustrated in Table II. For nondiagonal terms, G^R_{xy} is an odd function of $x - x'$ and $y - y'$, and a generalized even function of $z + z'$;

G^R_{xz} is an odd function of $x-x'$ and a generalized even function of $z+z'$; G^R_{yz} is an odd function of $y-y'$ and a generalized even function of $z+z'$. Therefore, the signs of the above nondiagonal components in all subdomains are easily obtained, as shown in Table II.

After defining the extended Green's functions, the object function $O^e(i_x, i_y, i_z)$ can be defined in the extended domain by zero padding

$$O^e(i_x, i_y, i_z) = \begin{cases} O(i_x, i_y, i_z), & \text{if } 0 \le i_{x,y,z} \le N_{x,y,z} - 1 \\ 0, & \text{else.} \end{cases} \tag{29}$$

Then, the right-hand side of (26) is exactly the cyclic convolution and correlation in the extended domain. Using the convolution theorem, (26) can be written as

$$A_{\xi\zeta}(i_x, i_y, i_z) = \frac{\Delta V}{4\pi\tilde{\epsilon}_b} C(i_x, i_y, i_z)\mathcal{F}^{-1}\left\{\tilde{G}^{Pe}_{\xi\zeta}(j_x, j_y, j_z)\tilde{O}^e(j_x, j_y, j_z) + \tilde{G}^{Re}_{\xi\zeta}(j_x, j_y, j_z)\tilde{O}^e(j_x, j_y, -j_z)\right\} \tag{30}$$

where $\tilde{G}^{Pe,\,Re}_{\xi\zeta}$ and $\tilde{O}^e$ are the discrete Fourier transforms of $G^{Pe,\,Re}_{\xi\zeta}$ and O^e, respectively. Obviously, this is an $O(N\log N)$ algorithm.

We remark that the formulation (30) is exact as is (26). Hence, the fast ExBorn algorithm gives exactly the same result as the conventional one. However, the computational complexity has been greatly reduced.

Generally, both the dyadic Green's functions $\overline{\mathbf{G}}^{bbP}_{ee}$ and $\overline{\mathbf{G}}^{bbR}_{ee}$ contain nine components. Hence, it requires 18 FFT and nine inverse FFT to evaluate the matrix $\overline{\mathbf{A}}$ from (30). Also, the memory requirement should be $18N$ to store the Green's functions. However, efficient formulations have been derived in Section II, where only $G^{P,\,R}_{xx}$, $G^{P,\,R}_{xy}$, $G^{P,\,R}_{xz}$, $G^{P,\,R}_{yy}$, $G^{P,\,R}_{yz}$, and $G^{P,\,R}_{zz}$ are independent. Hence, only 12 FFT and six inverse FFT are needed in the actual implementation, and the actual memory requirement is $12N$.

In the evaluation of the dyadic Green's functions, $G^P_{\xi\zeta}(i_x, i_y, i_z)$ is singular when $i_x = i_y = i_z = 0$ (i.e., the self-term). In 2-D case, closed-form expressions for the self-term of the polarization tensor have been given in terms of elementary functions [15]. In the 3-D case, if the discretization cell is a sphere, the closed-form solution for the self-terms has been derived in [10]. For the case of cubic cell, it has been shown that the self-term is nearly the same as that of spherical cell [10]. In the general case of cuboidal cell used in the fast ExBorn algorithm, a closed-form expression for $G^P_{\xi\zeta}(0, 0, 0)$ is given in the Appendix.

IV. CG-FFT Algorithm Based on Fast Exborn

The fast ExBorn algorithm provides a good approximation if the contrast of buried dielectric object is small or relatively large with respect to the lossy background at low frequencies, which will be seen in numerical examples in the next section. If the contrast is large, however, ExBorn becomes less accurate. In this case, the full-wave analysis based on the CG-FFT algorithm is a better choice to solve the problem accurately.

The CG-FFT method is much more efficient than MoM, as it requires only $O(N_{\text{iter}}N\log N)$ arithmetic operations [14], where N_{iter} is the number of CG iterations. For large problems, N_{iter} is much smaller than the number of unknowns, but still large for high-contrast objects. This is because the operator of the electric field integral equation (8) is not well conditioned at very low frequencies [19]. To improve the efficiency of such method, we incorporate the fast ExBorn with the CG-FFT algorithm.

As discussed in the above section, the ExBorn algorithm has provided a good approximation to the real solution of the electric field integral equation (8) or (32) or (15), although it is not very accurate for high-contrast objects. Hence, we propose a preconditioned CG-FFT algorithm based on the fast ExBorn to improve the efficiency of the conventional CG-FFT method. The combination of the ExBorn with the CG-FFT algorithm includes the following two issues.

- The solution of the fast ExBorn is chosen as the initial guess of CG-FFT.
- The inverse operator of the fast ExBorn is chosen as a preconditioner of CG-FFT.

The first issue is obvious because a good initial guess can accelerate the convergence of an iterative method. Now we discuss the second issue.

To solve the volume electric field integral equation using the CG-FFT method, we choose to use the compact form (14). For the equivalent electric current $\mathbf{J}_b$, the extended Born approximation (22) is rewritten as

$$\left[\overline{\mathbf{I}} + \overline{\mathbf{A}}(\mathbf{r}, \mathbf{r}_t)\right] \cdot \mathbf{J}_b(\mathbf{r}, \mathbf{r}_t) = \mathbf{J}^{\text{inc}}_b(\mathbf{r}, \mathbf{r}_t). \tag{31}$$

Hence, the electric field integral equation (14) can be written in an operator form

$$\overline{\mathbf{L}} \cdot \mathbf{J}_b = \mathbf{J}^{\text{inc}}_b \tag{32}$$

where the exact operator of the integral equation is given in (14). After discretizing the buried object using the regular mesh and extending the Green's functions, as discussed in Section III, the above operation can be performed using FFT

$$\overline{\mathbf{L}}_\xi \cdot \mathbf{J}_b = J_{b\xi}(i_x, i_y, i_z) + \frac{\Delta V}{4\pi}\chi(i_x, i_y, i_z)\mathcal{F}^{-1} \cdot \left\{\sum_{\zeta=x,\,y,\,z}\left[\tilde{G}^{Pe}_{\xi\zeta}(j_x, j_y, j_z)\tilde{J}_{b\zeta}(j_x, j_y, j_z) + \tilde{G}^{Re}_{\xi\zeta}(j_x, j_y, j_z)\tilde{J}_{b\zeta}(j_x, j_y, -j_z)\right]\right\}, \quad (\xi = x, y, z) \tag{33}$$

in which $G^{Pe,\,Re}_{\xi\zeta}$ are extended Green's functions defined before. Hence, the operator equation (32) can then be solved iteratively by using the CG-FFT method [11]–[14].

However, the exact operator $\overline{\mathbf{L}}$ of the electric field integral equation is not well conditioned at very low frequencies [19].

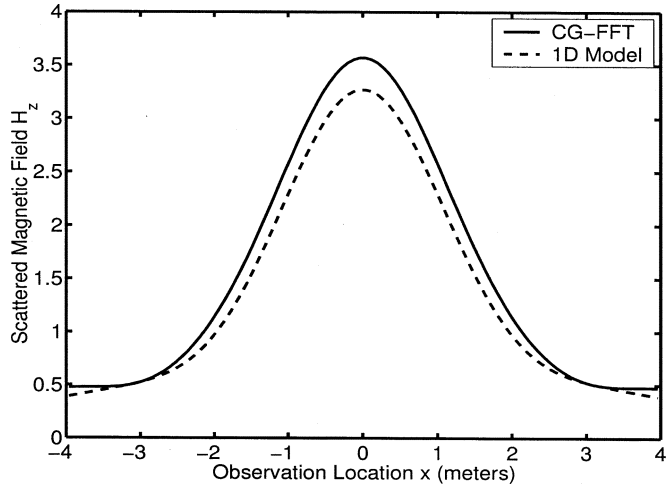

(a)

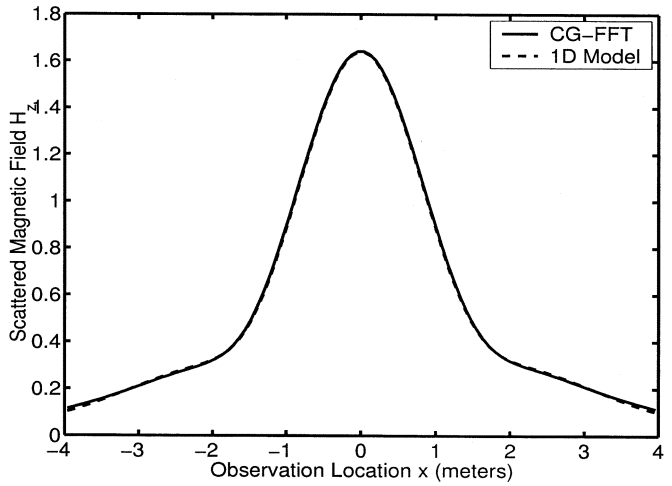

(b)

Fig. 2. Comparison of scattered magnetic fields of a buried dielectric cuboid using the preconditioned CG-FFT algorithm and the 1-D model under the excitation of a VMD. (a) $\epsilon_b = 10$, $\sigma_b = 0.02$ S/m, $\epsilon_s = 80$ and $\sigma_s = 0.16$ S/m. (b) $\epsilon_b = 10$, $\sigma_b = 0.1$ S/m, $\epsilon_s = 80$ and $\sigma_s = 0.8$ S/m.

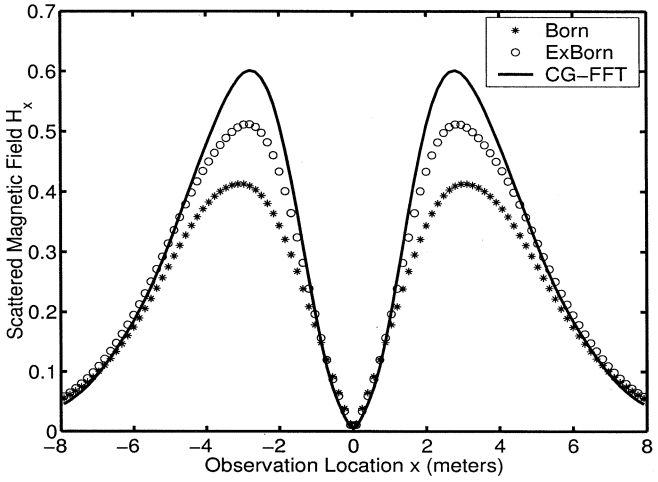

(a)

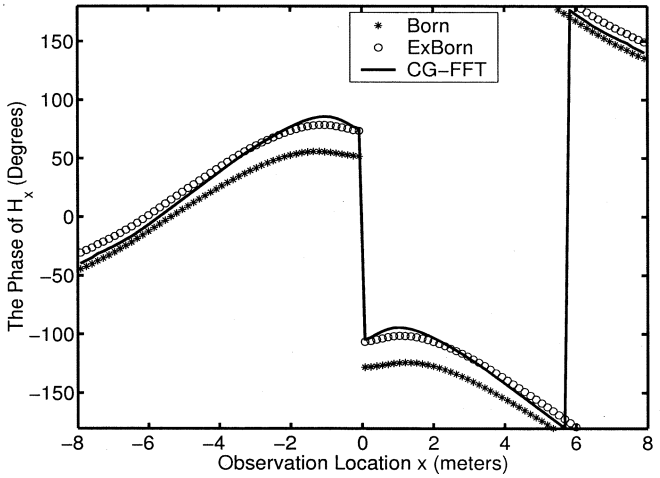

(b)

Fig. 3. Comparison of scattered magnetic fields (x components) of the buried dielectric cuboid under the excitation of a VMD when $\epsilon_b = 10$, $\sigma_b = 0.02$ S/m, $\epsilon_s = 40$ and $\sigma_s = 0.08$ S/m. (a) The amplitude. (b) The phase.

To improve the efficiency of the CG-FFT method, a preconditioner $\overline{\mathbf{P}}$ is used. Instead of solving (32) directly, we solve an equivalent problem

$$\overline{\mathbf{P}} \cdot \overline{\mathbf{L}} \cdot \mathbf{J}_b = \overline{\mathbf{P}} \cdot \mathbf{J}_b^{\text{inc}}. \tag{34}$$

The ideal preconditioner should be the inverse of the exact operator: $\overline{\mathbf{P}} = \overline{\mathbf{L}}^{-1}$. Then the product of operators $\overline{\mathbf{P}} \cdot \overline{\mathbf{L}}$ produces a unit operator, which has the minimum condition number. However, the inverse of the exact operator is very expensive to be performed, and is much more difficult than the operator itself. Hence, we choose the inverse of the approximate operator from the ExBorn as the preconditioner. From (31), we have

$$\overline{\mathbf{P}} = \overline{\mathbf{L}}_{\text{EB}}^{-1} = \left[\overline{\mathbf{I}} + \overline{\mathbf{A}}(\mathbf{r}, \mathbf{r}_t)\right]^{-1} \tag{35}$$

where the 3×3 matrix $\overline{\mathbf{A}}$ defined in (23) has been computed via FFT in the fast ExBorn algorithm and has been stored. We remark that the above preconditioner can be easily performed by inverting a 3×3 matrix. Comparing with the exact operator $\overline{\mathbf{L}}$, the approximate ExBorn operator $\overline{\mathbf{L}}_{\text{EB}}$ is equivalent to a block-diagonal operator. Hence, (35) is in fact a block-diagonal preconditioner, which can be easily performed at a low cost.

On the other hand, $\overline{\mathbf{L}}_{\text{EB}}$ is a good approximation of the exact operator $\overline{\mathbf{L}}$. Hence, the product of operators $\overline{\mathbf{L}}_{\text{EB}}^{-1} \cdot \overline{\mathbf{L}}$ is well conditioned. Considering the good initial guess from the fast ExBorn, the preconditioned CG-FFT algorithm based on (34) will converge much faster than the conventional CG-FFT algorithm.

V. Numerical Results

To test the validity and efficiency of the fast ExBorn and the ExBorn-based preconditioned CG-FFT algorithms, we consider a dielectric cuboid buried in the lossy earth. The cuboid has a size of $8 \times 8 \times 2$ m^3, which is partitioned by $32 \times 32 \times 8$ cubic cells. The top surface of the buried object is 1 m below the air–earth interface. The earth can be either lossy ($\sigma_b = 0.02$ S/m) or very lossy ($\sigma_b = 0.1$ S/m) with the relative permittivity $\epsilon_b = 10$ in both cases.

The transmitter is either a vertical magnetic dipole (VMD) or a vertical electric dipole (VED), which is 0.2 m above the

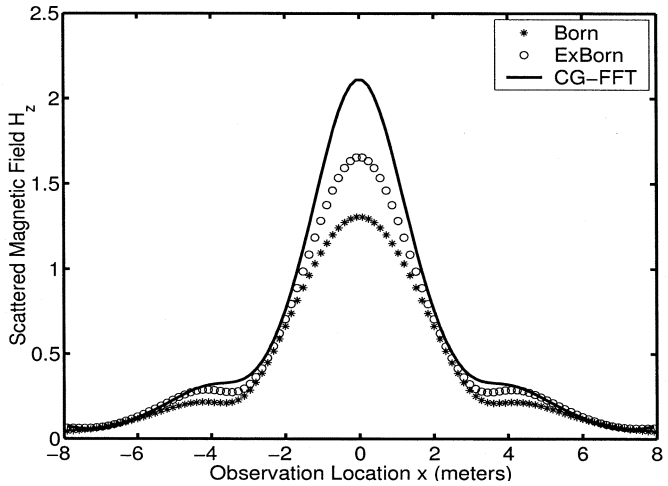

(a)

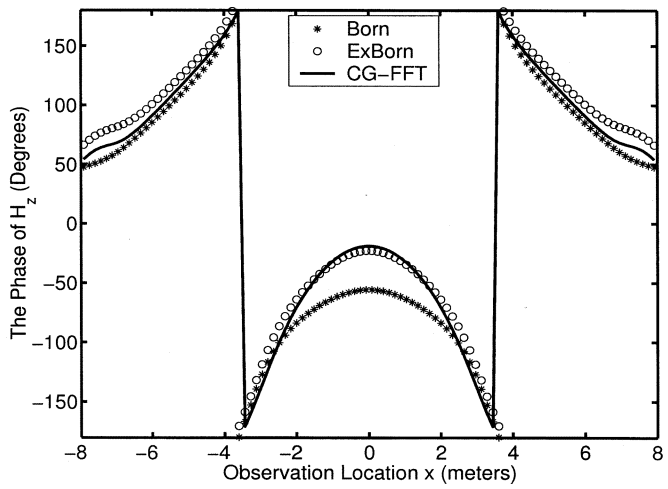

(b)

Fig. 4. Comparison of scattered magnetic fields (z components) of the buried dielectric cuboid under the excitation of a VMD when $\epsilon_b = 10$, $\sigma_b = 0.02$ S/m, $\epsilon_s = 40$ and $\sigma_s = 0.08$ S/m. (a) The amplitude. (b) The phase.

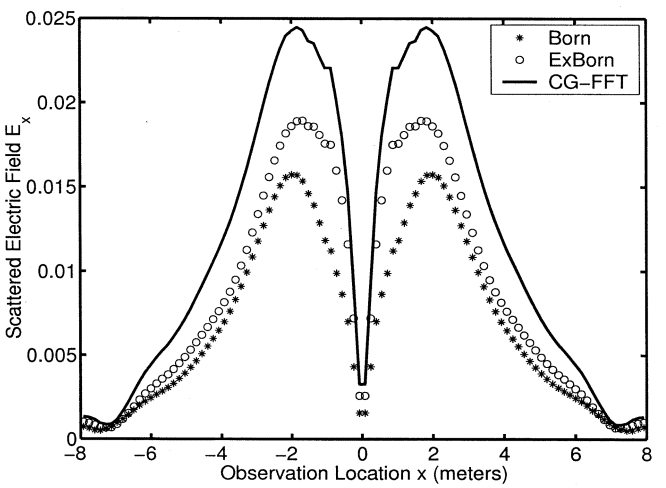

(a)

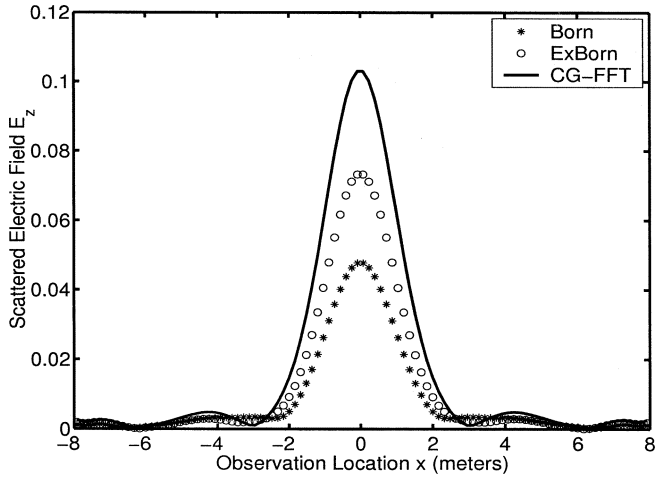

(b)

Fig. 5. Comparison of scattered electric fields (amplitudes) of the buried dielectric cuboid under the excitation of a VED when $\epsilon_b = 10$, $\sigma_b = 0.1$ S/m, $\epsilon_s = 40$ and $\sigma_s = 0.4$ S/m. (a) x component. (b) z component.

air–earth interface and is located at the center of the horizontal projection of the dielectric cuboid. In the following simulations, the working frequency is 5 MHz, and we choose $C(\mathbf{r}) = 1$ and $O(\mathbf{r}) = \tilde{\epsilon}_s(\mathbf{r}) - \tilde{\epsilon}_b$.

Because the vertical distance from the transmitter to the buried dielectric cuboid is much smaller than its horizontal size, we expect that the CG-FFT results from the proposed 3-D model will be very close to those from a 1-D model where the dielectric cuboid is infinite in its horizontal extension. In the 1-D model, it is in fact a four-layered problem: the first layer is the free space, the second layer is the lossy earth with thickness 1 m, the third layer is the buried dielectric cuboid with thickness 2 m, and the fourth layer is the lossy earth again. Closed-form solutions for the 1-D model can be found in [25].

When the dielectric cuboid is buried in the lossy earth ($\sigma_b = 0.02$ S/m) and has a contrast of $\epsilon_s = 80$ and $\sigma_s = 0.16$ S/m, the scattered magnetic fields have been computed using the preconditioned CG-FFT algorithm and the 1-D model under the excitation of VMD, as illustrated in Fig. 2(a). Here, the scattered fields are along a central line parallel to the x direction with respect to the buried target. From Fig. 2(a), we clearly see that the 3-D numerical result is very close to the 1-D analytical result.

When the dielectric cuboid is buried in the very lossy earth ($\sigma_b = 0.1$ S/m) and has a contrast of $\epsilon_s = 80$ and $\sigma_s = 0.8$ S/m, the comparison of scattered magnetic fields is depicted in Fig. 2(b) under the excitation of VMD. Clearly, the CG-FFT result is nearly the same as the 1-D analytical result. This is because the induced eddy current from VMD is concentrated in the center region of the cuboid when the earth is very lossy. The good agreement of simulation results from the two different models validates the preconditioned CG-FFT algorithm.

Now we compare the Born approximation, the fast ExBorn and preconditioned CG-FFT algorithms through several numerical examples. When $\epsilon_b = 10$, $\sigma_b = 0.02$ S/m, $\epsilon_s = 40$ and $\sigma_s = 0.08$ S/m, the scattered magnetic fields (both amplitudes and phases) computed by different methods are illustrated in Figs. 3 and 4, where the transmitter is a VMD. From Figs. 3 and 4, ExBorn is much more accurate than the Born approximation comparing with the full-wave CG-FFT analysis. In the

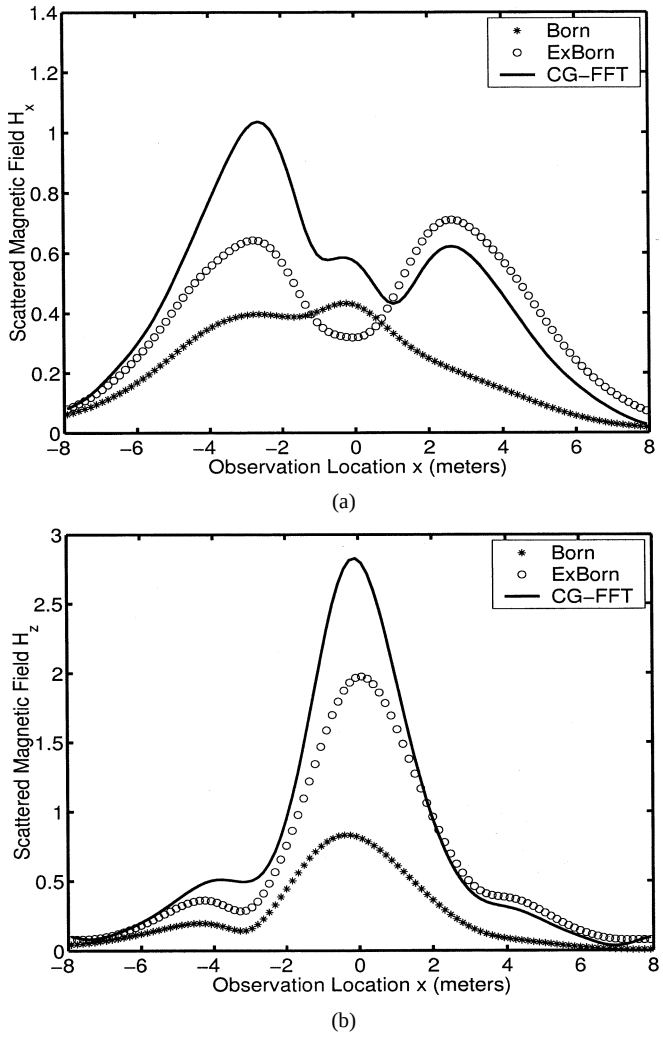

Fig. 6. Comparison of scattered magnetic fields (amplitudes) of the inhomogeneous dielectric cuboid under the excitation of a VMD when $\epsilon_b = 10$, $\sigma_b = 0.02$ S/m, $\epsilon_{s1} = 80$, $\epsilon_{s2} = 40$, $\sigma_{s1} = 0.16$ S/m, and $\sigma_{s2} = 0.08$ S/m. (a) x component. (b) z component.

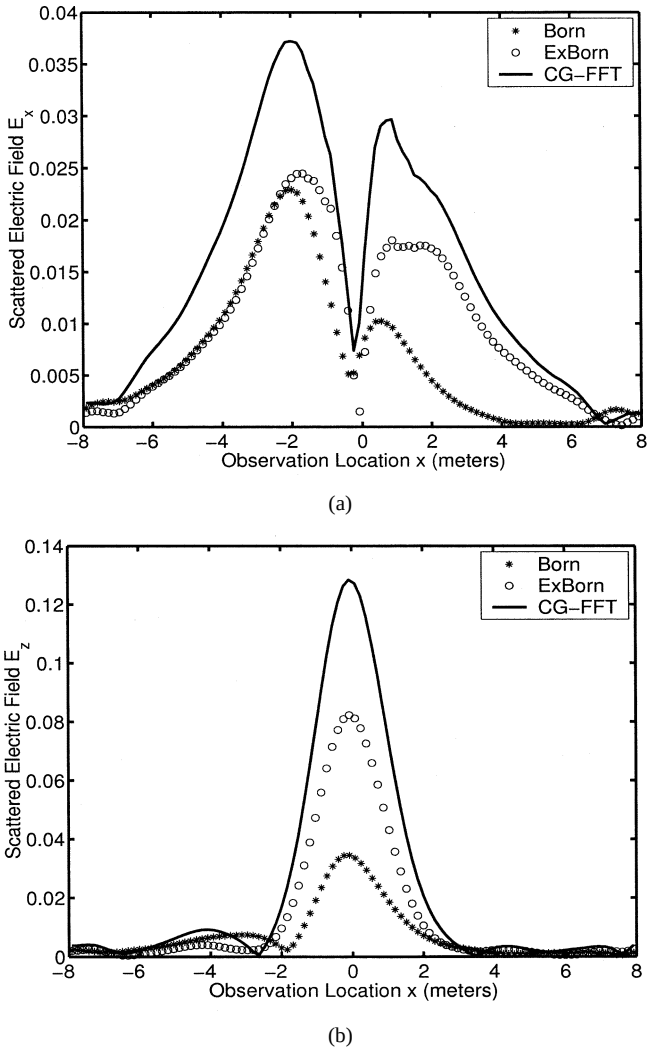

Fig. 7. Comparison of scattered electric fields (amplitudes) of the inhomogeneous dielectric cuboid under the excitation of a VED when $\epsilon_b = 10$, $\sigma_b = 0.1$ S/m, $\epsilon_{s1} = 80$, $\epsilon_{s2} = 40$, $\sigma_{s1} = 0.8$ S/m, and $\sigma_{s2} = 0.4$ S/m. (a) x component. (b) z component.

CG-FFT algorithm, 16 iterations have been used to reach the residual error of 0.000 07.

In the very lossy earth, when $\epsilon_b = 10, \sigma_b = 0.1$ S/m, $\epsilon_s = 40$ and $\sigma_s = 0.4$ S/m, the comparison of scattered electric fields (only the amplitudes for space reason) from the dielectric cuboid excited by a VED is shown in Fig. 5, where the Born approximation, the ExBorn and preconditioned CG-FFT algorithms have been used. Again, ExBorn is much more accurate than the Born approximation in the VED case. From Figs. 3–5, the field distributions along the observation line are symmetrical or antisymmetrical because of the homogeneity of the buried object.

Next we consider the scattering of the dielectric cuboid which is inhomogeneous in both conductivity and permittivity:

$$\sigma_s(x, y, z) = \begin{cases} \sigma_{s1}, & -4 \le x < 0 \\ \sigma_{s2}, & 0 \le x \le 4, \end{cases} \tag{36}$$

$$\epsilon_s(x, y, z) = \begin{cases} \epsilon_{s1}, & -4 \le x < 0 \\ \epsilon_{s2}, & 0 \le x \le 4. \end{cases} \tag{37}$$

When the inhomogeneous dielectric cuboid is buried in the lossy earth ($\epsilon_b = 10$ and $\sigma_b = 0.02$ S/m) and $\epsilon_{s1} = 80$, $\epsilon_{s2} = 40$, $\sigma_{s1} = 0.16$ and $\sigma_{s2} = 0.08$ S/m, the scattered magnetic fields computed by different methods are illustrated in Fig. 6 under the excitation of the VMD. From this figure, it is clear that ExBorn is much more accurate than the Born approximation comparing with the full-wave CG-FFT analysis even for inhomogeneous buried objects.

When the inhomogeneous cuboid is buried in the very lossy earth ($\epsilon_b = 10$ and $\sigma_b = 0.1$ S/m) and $\epsilon_{s1} = 80$, $\epsilon_{s2} = 40$, $\sigma_{s1} = 0.8$ and $\sigma_{s2} = 0.4$ S/m, the comparison of scattered electric fields computed by different methods is shown in Fig. 7, where the transmitter is the VED. Again, we observe that ExBorn is much more accurate than the Born approximation. Also, the field distribution along the observation line (in x direction) become asymmetrical because of the inhomogeneity of buried object in the x direction, as illustrated in Figs. 6 and 7.

VI. Conclusion

A fast ExBorn algorithm and a preconditioned CG-FFT method based on the fast ExBorn have been developed in this paper to study the electromagnetic scattering by 3-D dielectric

objects buried in the lossy earth. It has been shown that the fast ExBorn algorithm is much more accurate than the Born approximation at low frequencies and in the lossy case. Comparing with the full-wave analysis method, the fast ExBorn algorithm can provide good simulation results if the contrast of the buried object is small. If the contrast is large, however, the fast ExBorn becomes less accurate. In this case, a preconditioned CG-FFT algorithm is developed, where the solution of the fast ExBorn is chosen as the initial guess and the inverse operator of the fast ExBorn is used as the preconditioner. Comparing with the regular CG-FFT method, the preconditioned CG-FFT algorithm converges much faster.

APPENDIX

We consider a general cuboidal cell which has a size of $a_x \times a_y \times a_z$. Using the physical model proposed in [10], the self-terms $G^P_{\xi\zeta}(0, 0, 0)$ can be easily obtained. Generally, the self-terms are expressed by two integrals

$$\begin{aligned} &G^P_{\xi\xi}(0, 0, 0) \\ &\quad = 4\pi - 8a_\xi \left[K_1(\theta_\xi, a_{\xi_1}, a_\xi) + K_1\left(\frac{\pi}{2} - \theta_\xi, a_{\xi_2}, a_\xi\right)\right] \\ &\qquad + i4k_b a_\xi \left[K_2(\theta_\xi, a_{\xi_1}, a_\xi) + K_2\left(\frac{\pi}{2} - \theta_\xi, a_{\xi_2}, a_\xi\right)\right] \end{aligned} \tag{38}$$

$$\begin{aligned} &G^P_{\xi\zeta}(0, 0, 0) \\ &\quad = 0, \qquad (\zeta \neq \xi) \end{aligned} \tag{39}$$

in which the two integrals K_1 and K_2 are defined as

$$\begin{aligned} &K_1(\theta, a, b) \\ &\quad = \int_0^\theta e^{i\frac{1}{2}k_b\sqrt{a^2\sec^2\phi + b^2}} \Big/ \sqrt{a^2\sec^2\phi + b^2}\, d\phi \end{aligned} \tag{40}$$

$$\begin{aligned} &K_2(\theta, a, b) \\ &\quad = \int_0^\theta \int_0^1 e^{i\frac{1}{2}k_b\sqrt{a^2\sec^2\phi + b^2u^2}}\, du d\phi. \end{aligned} \tag{41}$$

Here, $\xi, \zeta = x, y, z$, $\theta_x = \tan^{-1} a_z/a_y$, $\theta_y = \tan^{-1} a_x/a_z$, and $\theta_z = \tan^{-1} a_y/a_x$. When $\xi = x$, ξ_1 and ξ_2 are y and z, respectively; when $\xi = y$, ξ_1 and ξ_2 are z and x, respectively; and when $\xi = z$, ξ_1 and ξ_2 are x and y, respectively. From (38), we clearly see that $G^P_{xx}(0, 0, 0) = G^P_{yy}(0, 0, 0) = G^P_{zz}(0, 0, 0)$ if the cell is a cube ($a_x = a_y = a_z$). In this case, we can easily show that the self-term (38) is nearly the same as that of a spherical cell with equal volume [10]. Using the general formulations (38) and (39), one can generate flexible meshes in the computational domain.

REFERENCES

[1] T. M. Habashy, R. W. Groom, and B. R. Spies, "Beyond the Born and Rytov approximations—A nonlinear approach to electromagnetic scattering," *J. Geophy. Res.*, vol. 98, pp. 1759–1775, Feb. 1993.

[2] L. Peters, J. J. Daniels, and J. D. Young, "Ground penetrating radar as an environmental sensing tool," *Proc. IEEE*, vol. 82, pp. 1802–1822, Dec. 1994.

[3] J. M. Bourgeois and G. S. Smith, "A fully three-dimensional simulation of ground penetrating radar: FDTD theory compared with experiment," *IEEE Trans. Geosci. Remote Sensing*, vol. 34, pp. 36–44, Jan. 1996.

[4] X. X. Zeng and McMechan, "GPR characterization of buried tanks and pipes," *Geophysics*, vol. 62, pp. 797–806, May 1997.

[5] L. Carin, N. Geng, M. McClure, J. Sichina, and L. Nguyen, "Ultra-wide-band synthetic-aperture radar for mine-field detection," *IEEE Antennas Propagat. Mag.*, vol. 41, pp. 18–33, Feb. 1999.

[6] W. C. Chew and Q. H. Liu, "Inversion of induction tool measurements using the distorted Born iterative method and CG-FFHT," *IEEE Trans. Geosci. Remote Sensing*, vol. 32, pp. 878–884, 1994.

[7] D. L. Wright, T. J. Cui, and W. C. Chew, "Progress on the very early time electromagnetic (VETEM) system," in *Proc. Ground Penetrating Radar (GPR'98)*. Lawrence, KS: The University of Kansas, May 27–30, 1998, pp. 159–164.

[8] T. J. Cui, W. C. Chew, A. A. Aydiner, D. L. Wright, and D. V. Smith, "Detection of buried targets using a new enhanced very early time electromagnetic (VETEM) prototype system," *IEEE Trans. Geosci. Remote Sensing*, vol. 39, pp. 2702–2712, Dec. 2001.

[9] P. E. Wannamaker, G. W. Hohmann, and W. A. SanFilipo, "Electromagnetic modeling of three-dimensional bodies in layered earths using integral equations," *Geophysics*, vol. 49, pp. 60–74, Jan. 1984.

[10] T. J. Cui, W. Wiesbeck, and A. Herschlein, "Electromagnetic scattering by multiple dielectric and conducting objects buried under multi-layered media, Part I: Theory; Part II: Numerical implementation and results," *IEEE Trans. Geosci. Remote Sensing*, vol. 36, pp. 526–546, Mar. 1998.

[11] M. F. Catedra, E. Gago, and L. Nuno, "A numerical scheme to obtain the RCS of three-dimensional bodies of resonant size using the conjugate gradient method and the fast Fourier transform," *IEEE Trans. Antennas Propagat.*, vol. 37, pp. 528–537, May 1989.

[12] P. Zwamborn and P. M. van dan Berg, "The three-dimensional weak form of the conjugate gradient FFT method for solving scattering problems," *IEEE Trans. Antennas Propagat.*, vol. 40, pp. 1757–1766, Sept. 1992.

[13] Q. H. Liu and W. C. Chew, "Applications of the CG-FFHT method with an improved FHT algorithm," *Radio Sci.*, vol. 29, no. 4, pp. 1009–1022, 1994.

[14] T. J. Cui and W. C. Chew, "Fast algorithm for electromagnetic scattering by buried 3D dielectric objects of large size," *IEEE Trans. Geosci. Remote Sensing*, vol. 37, pp. 2597–2608, Sept. 1999.

[15] C. Torres-Verdin and T. M. Habashy, "Rapid 2.5-dimensional forward modeling and inversion via a new nonlinear scattering approximation," *Radio Sci.*, vol. 29, no. 4, pp. 1051–1079, 1994.

[16] ——, "A two-step linear inversion of two-dimensional conductivity," *IEEE Trans. Antennas Propagat.*, vol. 43, pp. 405–415, Apr. 1995.

[17] ——, "Rapid numerical simulation of axisymmetric single-well induction data using the extended Born approximation," *Radio Sci.*, vol. 36, no. 6, pp. 1287–1306, 2001.

[18] T. J. Yu and L. Carin, "Analysis of the electromagnetic inductive response of a void in a conducting-soil background," *IEEE Trans. Geosci. Remote Sensing*, vol. 38, pp. 1320–1327, May 2000.

[19] W. Wu, A. W. Glisson, and D. Kajfez, "A study of two numerical solution procedures for the electric field integral equation at low frequency," *Appl. Comput. Electromagn. Soc. J.*, vol. 10, no. 3, pp. 69–80, Nov. 1995.

[20] Q. H. Liu and Z. Q. Zhang, "The hybrid extended Born approximation and CG-FFT method for electromagnetic induction problems," *IEEE Trans. Geosci. Remote Sensing*, vol. 39, pp. 347–355, Feb. 2001.

[21] H. W. Tseng, K. H. Lee, and A. Becker, "3D interpretation of electromagnetic data using a modified extended Born approximation," *Geophysics*, vol. 68, pp. 127–137, 2003.

[22] T. J. Cui and W. C. Chew, "Chapter 8: Fast forward and inverse scattering methods for objects buried underground," in *Fast and Efficient Algorithms in Computational Electromagnetics*, W. C. Chew, Ed. Norwood, MA: Artech House, July 2001, pp. 347–424.

[23] T. Isernia, V. Pascazio, and R. Pierri, "A nonlinear estimation method in tomographic imaging," *IEEE Trans. Geosci. Remote Sensing*, vol. 35, pp. 910–923, July 1997.

[24] V. Monebhurrun, D. Lesselier, and B. Duchene, "Evaluation of a 3-D bounded defect in the wall of a metal tube at eddy current frequencies: The direct problem," *J. Electromagn. Waves Appl.*, vol. 12, no. 3, pp. 315–347, 1998.

[25] W. C. Chew, *Waves and Fields in Inhomogeneous Media*, 2nd ed. New York: IEEE Press, 1995.

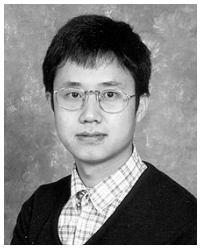

Tie Jun Cui (M'98–SM'00) was born in September 1965, in Hebei, China. He received the B.S., M.S., and Ph.D. degrees in electrical engineering from Xidian University, Xi'an, China, in 1987, 1990, and 1993, respectively.

In March 1993, he joined the Department of Electromagnetic Engineering, Xidian University, and was promoted to an Associate Professor in November 1993. From 1995 to 1997, he was a Research Fellow with the Institut für Höchstfrequenztechnik und Elektronik (IHE), University of Karlsruhe, Karlsruhe, Germany. In July 1997, he joined the Center for Computational Electromagnetics, Department of Electrical and Computer Engineering, University of Illinois at Urbana-Champaign, first as a Postdoctoral Research Associate and then a Research Scientist. In September 2001, he became a Professor with the Department of Radio Engineering, Southeast University, Nanjing, China, under the Cheung Kong Scholar Program awarded by the Ministry of Education, China. He is the author of three book chapters, over 80 scientific journal articles, and has presented over 20 conference papers. His research interests include wave propagation, scattering, inverse scattering, landmine detection, geophysical subsurface sensing, fast algorithms, and integrated circuit simulations.

Dr. Cui was awarded a Research Fellowship from the Alexander von Humboldt Foundation, Bonn, Germany, in 1995, received a Young Scientist Award from the International Union of Radio Science (URSI) in 1999, and received a Teaching Award from Southeast University, Nanjing, China, in 2003. He is a member of URSI (Commission B) and a Senior Member of the Chinese Institute of Electronics (CIE).

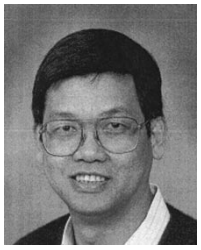

Weng Cho Chew (S'79–M'80–SM'86–F'93) was born in June 1953, in Malaysia. He received the B.S. degree in 1976, both the M.S. and Engineer's degrees in 1978, and the Ph.D. degree in 1980, all in electrical engineering. from the Massachusetts Institute of Technology, Cambridge.

From 1981 to 1985, he was with Schlumberger–Doll Research, Ridgefield, CT, first as a Program Leader and then a Department Manager. From 1985 to 1990, he was an Associate Professor with the University of Illinois, Urbana–Champaign. He is currently a Professor at the University of Illinois and teaches graduate courses in waves and fields in inhomogeneous media, and theory of microwave and optical waveguides and supervises a graduate research program. His name is listed many times in the *List of Excellent Instructors* on campus. He is the author of book *Waves and Fields in Inhomogeneous Media* (New York: Van Vostrand Reinhold, 1990; reprinted byIEEE Press, 1995), has published over 200 scientific journal articles, and has presented over 200 conference papers. His recent research interest has been in the area of wave propagation, scattering, inverse scattering, and fast algorithms related to scattering, inhomogeneous media for geophysical subsurface sensing, and nondestructive testing applications. Previously, he has also analyzed electrochemical effects and dielectric properties of composite materials, microwave and optical waveguides, and microstrip antennas. From 1989 to 1993, he was the Associate Director of the Advanced Construction Technology Center at the University of Illinois. Presently, he is the Director of the Center for Computational Electromagnetics and the Electromagnetics Laboratory at the same university. He is an Associate Editor of *Journal of Electromagnetic Waves and Applications* (1996–present) and *Microwave Optical Technology Letters* (1996–present). He was also an Associate Editor with the *International Journal of Imaging Systems and Technology* (1989–1994) and has been a Guest Editor of *Radio Science* (1986), *International Journal of Imaging Systems and Technology* (1989), and *Electromagnetics* (1995).

Dr. Chew is a member of Eta Kappa Nu, Tau Beta Pi, URSI Commissions B and F, and an active member with the Society of Exploration Geophysics. He was an NSF Presidential Young Investigator for 1986. He was also an AdCom member of IEEE Geoscience and Remote Sensing Society, and is presently an Associate Editor of the IEEE TRANSACTIONS ON GEOSCIENCE AND REMOTE SENSING (1984–present).

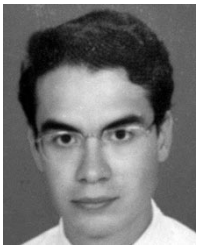

Alaeddin A. Aydiner (S'99) was born in Nazilli, Turkey on December 2, 1974. He received the B.S. degree from Bilkent University, Ankara, Turkey, in 1998, and the M.S. degree from the University of Illinois at Urbana-Champaign in 2000, both in electrical engineering. He is currently pursuing the Ph.D. degree at the University of Illinois.

Since August 1998, he is a Research Assistant in the Electromagnetics Laboratory, University of Illinois at Urbana–Champaign. His research interests include inverse problems, wave propagation in inhomogeneous media, and remote sensing.

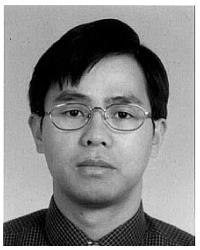

Yunhua H. Zhang (M'00) was born in Hunan province, China, in 1967. He received the B.S. from Xidian university, Xi'an, China, the M.S. and the Ph.D. degrees from Zhejiang University, Hangzhou, China, in 1989, 1993 and 1995, respectively, all in electrical engineering.

He joined the Center for Space Science and Applied Research, Chinese Academy of Sciences since September 1995, and he is currently a Professor there. From April to December 1998, he was a Senior Researcher at the Kwangju Institute of Science and Technology, Kwangju, Korea. From February 2001 to February 2002, he was a Postdoctoral Research Associate at the Center for Computational Electromagnetics, University of Illinois. His research interests cover the system design and signal processing of microwave sensors, such as radar altimeter, radar scatterometer, and synthetic aperture radar, as well as computational electromagnetics. He has developed many algorithms for the signal processing for the Chinese spaceborne multimode microwave sensors, which was launched at the end of 2002. He has been in charge of a national program for developing the imaging radar altimeter since 1998 (China).